International Journal of Hydrogen Energy 74 (2024) 170–182

Contents lists available at ScienceDirect

International Journal of Hydrogen Energy

journal homepage: www.elsevier.com/locate/he

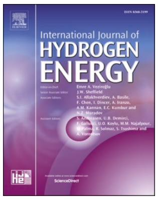

# Thermally activated dislocation motion in hydrogen-alloyed Fe–Cr–Ni austenitic steel revisited *via Haasen plot*

Yuhei Ogawa [a,b,*], Masaki Tanaka [c], Takeshi Fujita [d], Akinobu Shibata [a]

[a] *Research Center for Structural Materials, National Institute for Materials Science (NIMS), 1-2-1 Sengen, Tsukuba, 305-0047, Japan*
[b] *Department of Mechanical Engineering, Kyushu University, 744 Motooka, Nishi-ku, Fukuoka, 819-0395, Japan*
[c] *Department of Materials, Kyushu University, 744 Motooka, Nishi-ku, Fukuoka, 819-0395, Japan*
[d] *Graduate School of Engineering, Kyushu University, 744 Motooka, Nishi-ku, Fukuoka, 819-0395, Japan*

## ARTICLE INFO

Handling Editor: Suleyman I. Allakhverdiev

*Keywords:*
Austenitic steel
Hydrogen
Dislocation mobility
Thermal activation
Solute strengthening

## ABSTRACT

Enhancement of thermally activated dislocation motion by solute hydrogen (H) has been envisaged in Fe–Cr–Ni austenitic steel through accelerated stress relaxation and a prolonged creep duration. Nevertheless, differences in the imposed stress/strain between the compared non- and H-charged samples at the starts of these mechanical transients, as well as involvements of other obstacles (*e.g.*, alloying elements and forest dislocations), mask the essential effects of H. We performed stress relaxation and strain rate jump tests at multiple stress/strain for Type310S austenitic steel with ~7600 at ppm H at 296 K. The measured strain rate sensitivity (SRS) was evaluated *via* a methodology so-called *Haasen plot*. By screening the latent factors above, primary role of H was revisited: they work as short-range obstacles, hindering the dislocation movement. Multiple H atoms potentially participate in each thermal activation event, giving rise to a stress-equivalent activation volume and a proportionality between H concentration and yield strength.

## 1. Introduction

This paper provides the results of systematic transient mechanical tests for revisiting the roles of solute hydrogen (H) on thermally activated deformation in Fe–Cr–Ni austenitic steels. Despite the previous tenet of H-enhanced dislocation mobility under slow strain rate conditions [1,2], we prove that the intrinsic H-effect is to act as short-range obstacles like other alloying elements and invariably retard the dislocation motion. A potential model of H-dislocation interaction is proposed. The model successfully accounts for the characteristics of H-induced solid-solution hardening, which has been elucidated in the authors' previous work [3].

There is still an argument about whether solute H in metals enhances or inhibits the movement of dislocations depending on strain rate and temperature [2,4–17]. Enhancement of dislocation motion and softening of metals were first identified in H-charged iron and mild steel in the 1970s [7,8,18], later reproduced and elaborated [9,19–24]. Since the softening in iron was primarily observed around 200 K, it has been linked to facilitated kink-pair nucleation on screw dislocations with large Peierls barrier [7,21], a characteristic in metals with body-centered cubic (BCC) structure [25]. In contrast, in most of the face-centered cubic (FCC) materials, increases in yield stress, flow stress, and indentation hardness, or occurrence of serrated flow by H have been captured: Ni [4,26,27], Ni-alloys [5,28–30] and austenitic stainless steels [16,17,31–34]. This macro-scale fact contradicts the results of computational analyses and microscale experiments showing an accelerated dislocation motion even in FCC metals [2,10,11,35–38], stirring up a long-standing debate in the research field of H-dislocation interactions.

Birnbaum and Sofronis demonstrated the shielding of the stress field around an edge dislocation due to the formation of an H atmosphere [11]. While they used BCC-Nb as a model system for the simulation, their theory is applicable to FCC considering its simple assumption of size-effect for the solute-dislocation interaction. Because of the high diffusivity of H, the H atmosphere follow-up the movement of dislocation, giving rise to continuous stress shielding and increasing the dislocation mobility [39]. A similar result was reported numerically by Chateau and Delafosse in an austenitic steel, taking the H diffusion into account [35]. Some *in-situ* straining experiments in a transmission electron microscope (TEM) supported these analytical findings [9,10]. Although an argument has been made that the phenomenon observed in TEM is an artifact from the use of thin foil samples [40], changes in

---

[*] Corresponding author. Research Center for Structural Materials, National Institute for Materials Science (NIMS), 1-2-1 Sengen, Tsukuba, 305-0047, Japan.
*E-mail address:* OGAWA.Yuhei@nims.go.jp (Y. Ogawa).

https://doi.org/10.1016/j.ijhydene.2024.06.113
Received 25 April 2024; Received in revised form 30 May 2024; Accepted 9 June 2024

dislocation glide behavior after introducing $H_2$ gas in the observation chamber were directly visualized. The introduced H increased the dislocation velocity in Fe and Ni [9,10] and decreased the distance between pile-up dislocations in austenitic steel [36]. In addition to such a microscale standpoint, Birnbaum and Altstetter macroscopically substantiated an accelerated dislocation activity by H in FCC metals through stress relaxation, differential temperature, and creep experiments [1,2,41]. H in Ni and Type310S austenitic steel increased the amount of stress relaxation and the duration of creep, reducing the activation volume and enthalpy of plastic deformation. These insights were envisaged as critical evidence of enhanced thermally activated motion of dislocations by H *via* their weakened interaction with short-range obstacles [11]. Meanwhile, when the strain rate is so fast that the H atmosphere lags behind dislocation, an increase in strain rate sensitivity was reported [2]. Summarizing the assumptions established in these previous efforts, H may enhance the mobility of sluggishly moving dislocations, whereas it conversely retards rapidly moving dislocations.

A problem in these previous transient mechanical tests of austenitic steels is, however, that the behaviors in non-charged and H-charged specimens were compared at an identical strain or stress [1,2,16,41]. Because of the macroscopic hardening effect by solute H (*e.g.* Refs. [16,31]), the measurements at fixed stress and strain raise the differences in strain and stress, respectively, at the beginning of relaxation or creep. Stress relaxation rate and activation volume both depend on synergistic contributions from multiple short-range obstacles (*e.g.*, Peierls barrier, solute atoms), as well as on externally applied stress (*i.e.*, driving force for deformation) and strain (*i.e.*, forest dislocation density) [25,42–44]. Moreover, when relatively weak obstacles such as solutes, which can easily be thermally activated and more rate-sensitive, are involved, these obstacles may play a predominant role in determining the stress relaxation behavior [45]. The reduction in activation volume by adding alloying elements was indeed reported in solution-strengthened Al- and Ni-based FCC alloys [43,45,46], which is an equivalent tendency to the H-containing materials. Namely, the enhancement of stress relaxation and the decrease in activation volume reported so far [2,16] might capture some possible changes due to the involvement of a new type of short-range obstacle: H. Based on the stress relaxation and creep properties obtained under one stress/strain level alone, essential H-effects on the mobility of dislocations are not captured straightforwardly. Thus, a more dedicated methodology to extract the H-impact by subtracting other overriding factors is desired.

Mulford and Kocks [43,47–49] applied the method originally developed by Haasen [50] for decomposing the mechanisms determining the flow stress in FCC alloys. They measured the activation volume at multiple stress levels during tensile deformation, then plotted its inverse against flow stress: *Haasen plot*. The technique enables us to distinguish individual contributions from solution-strengthening [43,48], precipitation-hardening [43,51], strain-hardening [48–50], and dynamic recovery [49] on thermally activated deformation. Besides, it can capture dynamic interactions between dislocations and diffusible solute atoms [47,52]. In the present study, this methodology was adopted for a Fe–Cr–Ni-based austenitic steel uniformly charged with ~7600 at ppm solute H. Transient mechanical tests (*i.e.*, stress relaxation and strain rate jump tests) were carried out to revisit the roles of solute H on thermally activated dislocation motion in the Fe–Cr–Ni alloy system employing the Haasen plot.

## 2. Theoretical background

The construction of Haasen plot requires two mutually interrelated parameters at various stress levels: activation volume and strain rate sensitivity (SRS). This section provides the physical meaning and experimental measurements of those parameters, describing an interpretation of Haasen plot.

### 2.1. Physical description

Considering the movement of dislocations with getting held up by short-range obstacles on the slip plane, the plastic shear strain rate can be written as [25,42]:

$$\dot{\gamma} = \dot{\gamma}_0 \exp\left(-\frac{\Delta G}{kT}\right) \tag{1a}$$

or

$$\Delta G = kT \ln\left(\frac{\dot{\gamma}_0}{\dot{\gamma}}\right) = kT(\ln \dot{\gamma}_0 - \ln\dot{\gamma}) \tag{1b}$$

Here, $\dot{\gamma}_0$ [1/s] is a structural factor involving the vibrational frequency of the dislocation segment, mobile dislocation density, $\rho_m$, and average interspacing between dispersed obstacles on the slip plane. $k$ is the Boltzmann constant, $T$ is temperature, and $\Delta G$ is a change of Gibbs free energy when a dislocation surmounts an obstacle by thermal vibration [53]. $\Delta G$ is a function of activation energy at zero stress, $\Delta G_0$, and the thermal component of shear stress, $\tau^*$: $\Delta G = \Delta G_0 - \tau^* V$. The parameter $V$ is

$$V = -\frac{\partial \Delta G}{\partial \tau^*} \tag{2}$$

which is the so-called activation volume [42], a product of Burgers vector, $b$ ($\approx 2.5 \times 10^{-10}$ m), the extent of an obstacle, $d$, and the obstacle interspacing, $L$. $V$ corresponds to the area swept by a dislocation during each thermal activation event, $dL$ (activation area), multiplied by $b$: $V = bdL$ [25,53]. Incorporating eq. (1b) into eq. (2), strain rate and activation volume are interrelated as

$$S = \frac{\partial \tau^*}{\partial \ln\dot{\gamma}} = \frac{kT}{V} \tag{3}$$

where $S$ is SRS, a parameter inversely proportional to $V$.

### 2.2. Measurement of activation volume and strain rate sensitivity

A general method to experimentally measure activation volume is the stress relaxation test [2,42,54,55]. During a uniaxial tensile deformation, the machine crosshead is fixed for a timeframe, the stress drop during which is recorded. Under a constant crosshead displacement, the elastic strain of the specimen-machine assembly is gradually replaced by the plastic strain of the specimen's gauge part. Groh and Conte proposed an equation that correlates the relaxation stress drop, $\Delta\tau$ (a negative quantity), to the relaxation time, $t$, assuming a constant activation volume during the relaxation period [54].

$$\Delta\tau = -\frac{kT}{V_a}\ln\left(\frac{t}{c}+1\right) \tag{4}$$

where $c$ is a time constant, and $V_a$ is an apparent activation volume. The $\Delta\tau$ in eq. (4) can involve not only the decay of effective stress, $\Delta\tau^*$ (release of elastic strain), stemming from thermally activated movement of dislocations, but also the flow stress-increase due to an increasing plastic strain during the relaxation, $\Delta\gamma_p$, and resultant strain-hardening (*i.e.*, $\Delta\tau = \Delta\tau^* + \theta\Delta\gamma_p$, where $\theta$ is strain-hardening rate). Thus, $V_a$ also involves its strain-hardening component, $V_h$, in addition to the true physical activation volume related purely with $\Delta\tau^*$, $V$ (*i.e.*, $V_a = V + V_h$).

For measuring physical activation volume, $V$, the repeated stress relaxation test was invented by Spätig et al. [55,56]. According to their methodology, the stress is reverted to the original level after a relaxation; then, the specimen is relaxed again for the same period as the previous relaxation. This procedure is repeated 4–6 times. The deformation during the stress reversion should be quasi-elastic [55]. Therefore, the SRS ($S$) and activation volume ($V$), excluding the strain-hardening effect, can be determined.

$$S = \frac{\Delta\tau_j}{\ln\left(\dot{\gamma}_{(j+1)i}\Big/\dot{\gamma}_{jf}\right)} = \frac{kT}{V} \tag{5}$$

where $\Delta\tau_j$ is the stress drop in $j$th relaxation, $\dot{\gamma}_{jf}$ is the strain rate at the end of $j$th relaxation, and $\dot{\gamma}_{(j+1)i}$ is the strain rate at the beginning of ($j$+1) th relaxation. Presuming a constant $\dot{\gamma}_0$ (*i.e.*, constant $\rho_m$) in the quasi-elastic stress reversion, eq. (5) provides the stress-dependence of dislocation velocity. Practically, the stress-time relationship in the first relaxation is fitted with eq. (4) for determining $V_a$, then eq. (5) is applied to the following relaxations. This procedure finally gives the strain-hardening component, $V_h$.

$$(n-1)V_h = \frac{kT}{\overline{\Delta\tau}}\ln\left\{\frac{\exp\left(-\frac{\Delta\tau_n}{\lambda}\right)-1}{\exp\left(-\frac{\Delta\tau_1}{\lambda}\right)-1}\right\} \tag{6}$$

In eq. (6), $n$ is the total number of relaxations, $\overline{\Delta\tau}$ is the average of the stress drops in first ~($n$-1)th relaxations, and $\lambda = kT/V_a$. The right-hand side of eq. (6) is plotted versus ($n$-1), a slope of which gives $V_h$.

SRS and $V$ can more easily be measured by strain rate jump test [42,53,55]. If the strain rate is rapidly increased from $\dot{\gamma}_1$ to $\dot{\gamma}_2$ in a continuous deformation, and the flow stress is accordingly increased by $\Delta\tau$, $S$ and $V$ are given as

$$S = \frac{\Delta\tau}{\ln(\dot{\gamma}_2/\dot{\gamma}_1)} = \frac{kT}{V} \tag{7}$$

Note, however, that the $S$ and $V$ determined in this method may include the influence of dislocation multiplication due to the prompt stress increase [55]. Therefore, the repeated stress relaxation test is more appropriate for measuring $S$ and $V$ since the quasi-elastic deformation during the stress reversion can also exclude such an undesirable effect.

### 2.3. *Interpretation of Haasen plot*

If the flow stress is expressed by linear superposition of the intrinsic frictional strength of the matrix, $\tau_y$, and the strain-hardening, $\tau_d$ (*i.e.*, $\tau = \tau_y + \tau_d$) [48,57], $S$ also becomes a simple sum of the derivatives of each component: $S_y$ and $S_d$.

$$S = S_y + S_d = \frac{\partial\tau_y}{\partial\ln\dot{\gamma}} + \frac{\partial\tau_d}{\partial\ln\dot{\gamma}} = \frac{\partial\tau_y}{\partial\ln\dot{\gamma}} + \frac{\partial\ln\tau_d}{\partial\ln\dot{\gamma}}\tau_d = \frac{\partial\tau_y}{\partial\ln\dot{\gamma}} + \frac{\partial\ln\tau_d}{\partial\ln\dot{\gamma}}\left(\tau - \tau_y\right) \tag{8a}$$

or

$$S = \left(\frac{\partial\ln\tau_y}{\partial\ln\dot{\gamma}} - \frac{\partial\ln\tau_d}{\partial\ln\dot{\gamma}}\right)\tau_y + \frac{\partial\ln\tau_d}{\partial\ln\dot{\gamma}}\tau \tag{8b}$$

Accordingly, the inverse of their activation volume can be written as

$$\frac{1}{V} = \frac{1}{V_y} + \frac{1}{V_d} \tag{9}$$

In the Haasen plot, $S$ or inverse of $V$ (eq. (3)) is plotted against $\tau - \tau_y$ or $\tau$, where $\tau_y$ is often approximated by yield (0.2% proof) stress [46,48]. The intercept and the slope of the Haasen plot reflect the frictional and strain-hardening (*i.e.*, interaction between mobile and forest dislocations) components of $S$ and $V$, respectively. Given that the strain-hardening component of the activation volume is $V_d$, $\tau_d$ is expressed as follows according to the Bailey-Hirsch equation [58].

$$\tau_d = \alpha\mu b\sqrt{\rho_f} \approx \alpha\mu b\frac{1}{L_d} \propto \alpha\mu b\frac{1}{V_d} \tag{10}$$

where $\alpha$ is a material constant around ~0.5 [49,59], and $\mu$ is the shear modulus. $\rho_f$ is forest dislocation density on the slip plane, and $L_d$ is their average interspacing. From eqs. (3) and (8)~(10), $S_d$ and $1/V_d$ are both proportional to $\tau_d$. Thus, $S$ or $1/V$ vs. stress plot generally becomes a straight line: Cottrell-Stokes law [48–50,60]. An experimental acquisition of the Haasen plot isolates the SRS and activation volume into frictional and dislocation interaction components. This enables us to identify the impacts of solute H on each component of $S$ and $V$, although the Haasen plot slope can also be influenced by the presence of solutes [43,45], as later explained in Section 5.4.

## 3. Experimental methods

### 3.1. *Material and specimen*

Type310S austenitic stainless steel, the H-effects on the deformation behavior of which has been investigated in the past [2,3,16,17,31,61], was used in this study. The chemical composition of the steel is 0.02C-0.37Si-1.10Mn-0.023P-0.001S-19.18Ni-24.18Cr (mass %) balanced with Fe. A hot-forged bar of 20 mm-diameter was solution-treated at 1353 K and quenched in water, resulting in a fully austenitic microstructure with a grain size of 30~70 μm (see Appendix A1 for the microstructural image). Dog bone-shaped cylindrical tensile specimens with a diameter of 6 mm and a 30 mm gauge length (details can be found in Refs. [[16],17]) were machined parallel to the axis of the round-bar material, and the surface of their gauge section was mirror-finished by polishing with 1 μm diamond suspension.

### 3.2. *Hydrogen charging*

The tensile specimens were H-charged in $H_2$ gas at 543 K for 200 h. These temperatures and exposure time are sufficient to achieve a saturation of H in the gauge part of the specimens with a 6 mm diameter [16,17]. The gas pressures for charging were 10, 40, and 100 MPa, each giving rise to different H concentrations (Appendix A2). The H-charged specimens were preserved at 190 K until the start of mechanical tests.

Cylindrical samples with 5 mm height were cut from the deformed specimens, the H concentrations of which were measured by thermal desorption analysis (TDA) under a 100 K/h heating rate. A gas chromatography system equipped with a thermal conductivity detector (J-SCIENCE LAB, JTF-20 A series) was employed for TDA. Considering the bulk H diffusivity, $D$, in Type310S steel, the desorption of H from the specimen surface at ambient temperature should be limited to a thin layer of less than 10 μm [61]. The fraction of lost H during the mechanical tests is negligible as compared to the total residual amount of H.

### 3.3. *Transient mechanical tests*

Repeated stress relaxation tests were performed at 296 K with the base crosshead speed of $3 \times 10^{-3}$ mm/s (base strain rate of $10^{-4}$/s). A screw-driven electromechanical test frame with 100 kN load capacity, Shimadzu AGX-plus, was employed for the experiments. In addition, strain rate jump tests were carried out with the base crosshead speeds of $3 \times 10^{-4}$ mm/s (base strain rate of $10^{-5}$ 1/s). More test details and the reason for using different base strain rates will be described later. A contact-type strain gauge extensometer with a gauge length of 24 mm was attached to the specimen's parallel part for the measurement of tensile strain. The temperature fluctuation in the experimental room was regulated within ±1 K in order to ensure high thermal stability during the measurements. As the reference for these transient tests, monotonic tensile tests were also conducted at the strain rates of $10^{-4}$ 1/s and $10^{-5}$ 1/s. The tensile stress and strain were translated into shear stress and strain considering the Taylor factor of polycrystalline FCC metals: $M = 3.06$.

The repeated stress relaxation test explained in Section 2.2 [56] was done at multiple stress levels during the tensile deformation. In order to confirm the reproducibility, the experiment was duplicated for each H concentration. Type310S austenitic steel exhibits deformation twinning prior to necking around 0.25 true strain [16,61]. Thus, the stress relaxation measurement was confined to ~0.2 true strain, where plasticity is thoroughly carried by dislocation activity. For each stress level, the relaxation was repeated five times, and the individual relaxation was continued for 30 s. Before the stress relaxation tests, the elastic modulus of specimen-machine assembly, $E_{el}$, was measured as the load-crosshead displacement relationship to calculate the plastic strain rate during relaxation: $\dot{\varepsilon}_{Pl} = -\dot{P}/E_{el}l_s$, where $\dot{P}$ is the load reduction rate, and $l_s$ is the specimen's gauge length. Additionally, for an improvement in experimental accuracy, the machine relaxation under the loads identical to the stress relaxation tests was also measured for 30 s and subtracted from all the relaxation curves. Note that the machine relaxation was quite small compared with the total relaxation stress drop. The measurement of machine relaxation was realized by using a material (Ni-based alloy, UNS-N07718) that does not yield under the stress range in this study and possesses an elastic modulus similar to austenitic steels.

Strain rate jump tests were similarly conducted at various stress levels until the true strain reached 0.2. A ten-fold escalation of the crosshead speed from the base value (*i.e.*, from $10^{-5}$ to $10^{-4}$ 1/s) was interposed. The flow stress increase immediately after the strain rate jump was measured.

### 3.4. Characterization of dislocation structures

For a fair evaluation of H-effects on the mobility of individual dislocations under a given deformation condition, internal structures should not so differ due to the presence of H. In order to confirm this, dislocation structures in non-charged and H-charged specimens were characterized by TEM (JEOL, JEM-2100) operated at an acceleration voltage of 200 kV. A 3 mm disk was cut from the specimens deformed to 0.05 and 0.20 nominal tensile strains (0.049 and 0.182 true strains) under a strain rate of $10^{-4}$/s so that the disk plane was perpendicular to the tensile axis. The center part of the disk was thinned until a hole is open by twin-jet electrochemical polishing with an electrolyte of 10% perchloric acid and 90% ethanol.

## 4. Results

### 4.1. Hydrogen concentration and tensile flow behavior

The TDA revealed that the average H concentration, $C_0$, was 2140, 3920, and 7640 at ppm for specimens charged at 10, 40, and 100 MPa, respectively. These values well reproduce our previous measurements on the same Type310S steel charged under the conditions identical to the present study [3]. The H concentration significantly increased from the non-charged state (270 at ppm). The $C_0$ followed Sievert's law [62] (Appendix A2), indicating that H atoms primarily dissolved into interstitial lattice sites (*i.e.*, octahedral sites in FCC) before the specimens were deformed.

Fig. 1 (a) shows the nominal tensile stress-strain curves of the specimens H-charged at 100 MPa $H_2$ gas, as well as of non-charged specimens under two different strain rates. The yield and flow stresses were increased with an increase in strain rate, and the H-charged specimens also exhibited H-induced enhancement of flow stress at both strain rate conditions. The increase of flow stress due to solute H was also a monotonic function of the charging pressure (H concentration), although the results are not included in Fig. 1 (a). For the detailed influence of H concentration on the flow behavior, the readers shall refer to Appendix A2 or the author's previous publication [3].

The true stress-strain and strain-hardening rate curves of the same specimens in Fig. 1 (a) are represented in Fig. 1 (b). In the following, true stress and true strain are used rather than nominal stress and strain throughout the paper, unless otherwise noted. When the strain was greater than 0.2, the strain-hardening rate of H-charged specimens became larger than those of non-charged specimens. This effect is due to deformation twinning and its enhancement by solute H [16,61]. Conversely, the presence of H temporarily decreased the strain-hardening rate at the strain below 0.1.

### 4.2. Dislocation structures

The bright-field TEM images are shown in Fig. 2 for non-charged and H-charged (7640 at ppm) specimens deformed to 0.05 and 0.20 nominal strains (0.049 and 0.182 true strains). The tensile axis of the observed grains was almost parallel to [011] for the samples strained to 0.05, while it was close to [001] for 0.20 strain. At 0.05 strain (Fig. 2 (a) (b)), isolated dislocations formed planar arrays in some regions in the micrographs. Meanwhile, dislocations were heavily tangled and organized into cell structures for a larger strain of 0.20 (Fig. 2 (c) (d)). Importantly, no meaningful difference was found in the dislocation arrangements between non-charged and H-charged samples.

### 4.3. Effects of solute H on thermally activated deformation

Fig. 3 shows stress-strain curves in (a) repeated stress relaxation and (b) strain rate jump tests of non-charged and H-charged (7640 at ppm) specimens at the base strain rates of (a) $10^{-4}$/s and (b) $10^{-5}$/s. The general H-effects on thermally activated deformation are now figured out.

At a strain of around 0.05, H increased the magnitude of stress relaxation (inset of Fig. 3 (a)). The corresponding activation volumes, $V$, were $197b^3$ and $87b^3$ in non-charged and H-charged specimens, respectively. For checking the accuracies of data fitting by eq. (4) and the derivation of $V_h$ by eq. (6), the readers shall refer to Appendix A3.

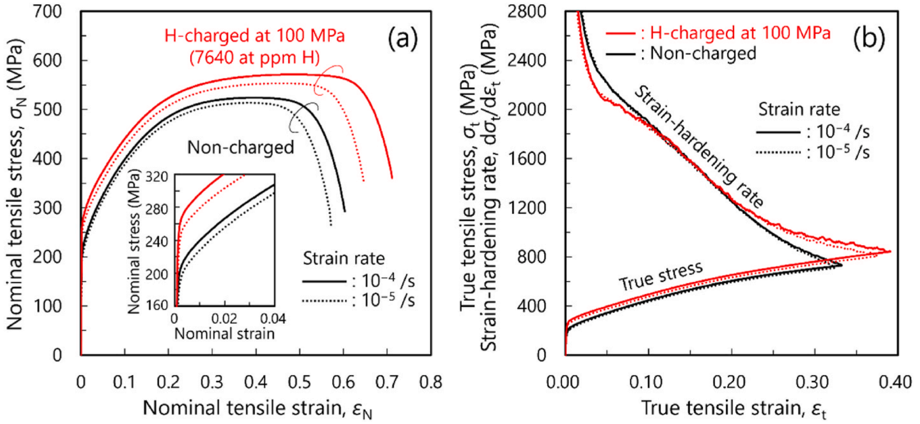

**Fig. 1.** (a) nominal and (b) true stress-strain curves of non-charged and H-charged (7640 at ppm) specimens at two different strain rates. The strain-hardening rate curves are also included in (b). The inset in (a) enlarges the behavior around the yield points.

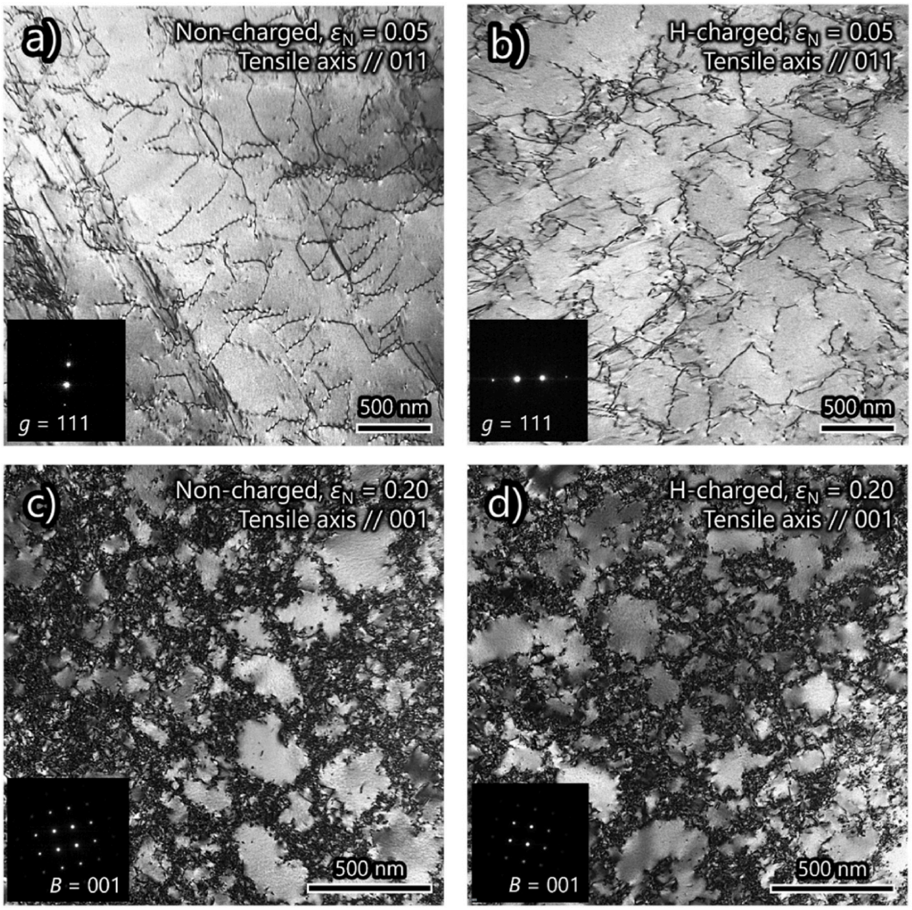

**Fig. 2.** Bright-field TEM micrographs of the dislocation structures in (a) (c) non-charged and (b) (d) H-charged (7640 at ppm) specimens deformed to (a) (b) 0.05 and (c) (d) 0.20 nominal tensile strains (0.049 and 0.182 true strains) with the strain rate of $10^{-4}$/s. The tensile axes of the captured grains were (a) (b) [011] and (c) (d) [001]. (a) and (b) were acquired in two-beam conditions with the diffraction vector, $g = 111$, while the beam direction, $B$, close to 001 zone axis was used for (c) and (d). The corresponding selected area electron diffraction patterns are shown in the insets.

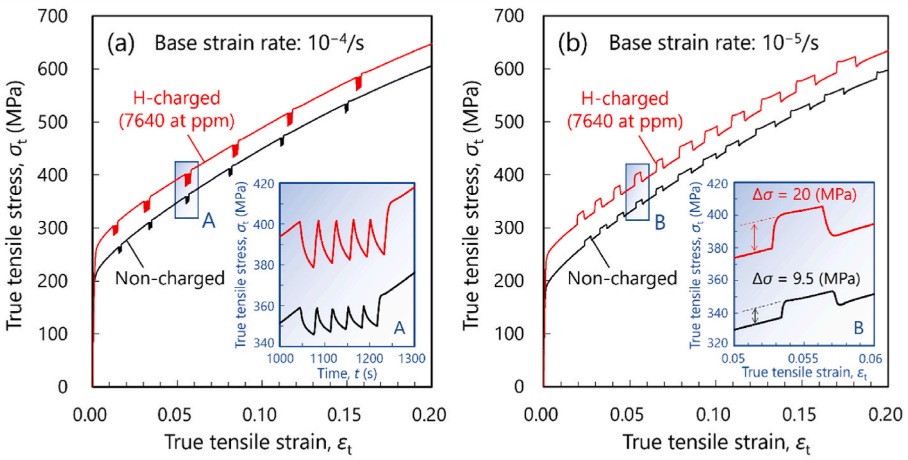

**Fig. 3.** True tensile stress-strain curves of non-charged and H-charged (7640 at ppm) specimens in (a) stress relaxation and (b) strain rate jump tests with the base strain rates of (a) $10^{-4}$/s and (b) $10^{-5}$/s, respectively. The insets in (a) and (b) magnify the rectangles A and B, wherein time is used as the horizontal axis of A instead of strain.

These qualitative H-effects were monotonically amplified with the increase in H concentration. Examples of the H concentration-effect on the stress drop during the first relaxation in each relaxation series, $\Delta\tau_1$, and on activation volumes (*i.e.*, $V_a$ and $V$) are depicted in Fig. 4. In all the specimens and stress levels, $V_a$ was slightly larger than $V$ due to its strain-hardening component, $V_h$. Additionally, the magnitude of $\Delta\tau_1$ almost linearly increased with the increase in stress in the non-charged specimen (Fig. 4 (a)), *i.e.*, Cottrell-Stokes law [49,50] obeyed. Besides an obvious dependence of $V$ on the applied stress under both the presence and absence of H, the large decreases of $V$ by solute H were evident.

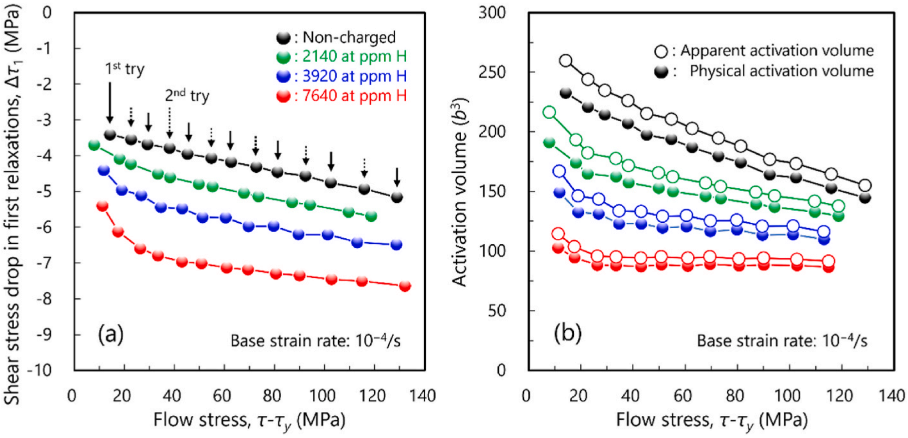

**Fig. 4.** Effects of solute H concentration on (a) the magnitude of stress-drop during the first relaxation in each relaxation series and (b) apparent as well as physical activation volumes as a function of flow stress. The imposed base strain rate was $10^{-4}$/s.

In Fig. 5 (a), the plastic strain rate, $\dot{\varepsilon_{Pl}}$, during the first relaxation in each relaxation series is presented. Yet $\dot{\varepsilon_{Pl}}$ were roughly calculated from the stiffness of specimen-machine assembly (Section 3.3), the coincidence between $\dot{\varepsilon_{Pl}}$ at the beginning of relaxation and relevant base strain rate [42] indicates the validity of $\dot{\varepsilon_{Pl}}$. Irrespective of the applied strain, $\dot{\varepsilon_{Pl}}$ transitioned from $10^{-4}$ to $10^{-5}$/s. This range was not largely changed in the following 2nd~5th relaxations, as an example at ≈ 0.05 strain is shown in Fig. 5 (b). This strain rate range of $10^{-4}$~$10^{-5}$/s in relaxation was the reason why we used the strain rate jump from $10^{-4}$ to $10^{-5}$/s: the strain rate conditions in the two types of tests were unified each other. As can be inferred from the increase in stress drop (Fig. 4 (a)), H apparently accelerated the plastic strain rate during relaxation under a given strain. On the other hand, Fig. 3 (b) indicates that solute H amplified the stress escalation at the strain rate jump, clarifying the H-induced increase of SRS.

All the H-effects listed above (*i.e.*, enhancements of flow stress, stress relaxation, plastic strain rate during stress relaxation, and SRS, as well as the reduction in activation volume) well reproduce the findings established in the past [2,16,31,41]. The (i) enhancement of stress relaxation (*i.e.*, reduction in activation volume) and the (ii) increase in SRS have been taken as the evidence for the two contradicting roles of solute H on dislocations activity: H accelerates the slow movement of dislocations, while H retards their rapid motion [2,16] (cf. Section 1). Nevertheless, one has to be aware that these two facts, (i) and (ii), have an identical physical meaning because there is an inverse correlation between activation volume and SRS (cf. eq. (3)). This notion makes the authors re-examine the assumption on such dislocation velocity-dependent dual roles of solute H. The novelty of the present research lies in how these experimental facts are interpreted when the Haasen plot is employed for the data evaluation.

### 4.4. Haasen plot

Fig. 6 (a) shows the SRS, *i.e.*, the inverse activation volume (eq. (3)), as a function of flow stress (Haasen plot) under various H concentrations measured in stress relaxation tests. The horizontal axis was taken as $\tau - \tau_y$ (cf. eq. (8a)). Note that each curve was constructed from two specimens so that their data points are alternately lined up. As expected from eq. (8a), a linear plot with a positive intercept and slope was obtained in the non-charged specimen (Fig. 6 (a)), while the slope was somewhat shallow as compared with pure FCC metals [43,49,50] (*e.g.*, the slope is $10^{-2}$ order for pure Ni). These positive intercepts and shallow slopes are due to the presence of alloying elements in the present steel (*e.g.*, 24 mass%-Cr and 19 mass%-Ni (refer to Section 3.1)). They might act as more thermally activatable obstacles than forest dislocations, primarily dominating the stress relaxation behavior [43,45,48].

The Haasen plot of H-charged specimens exhibited a distinct behavior, in which the difference became more apparent as the H con-

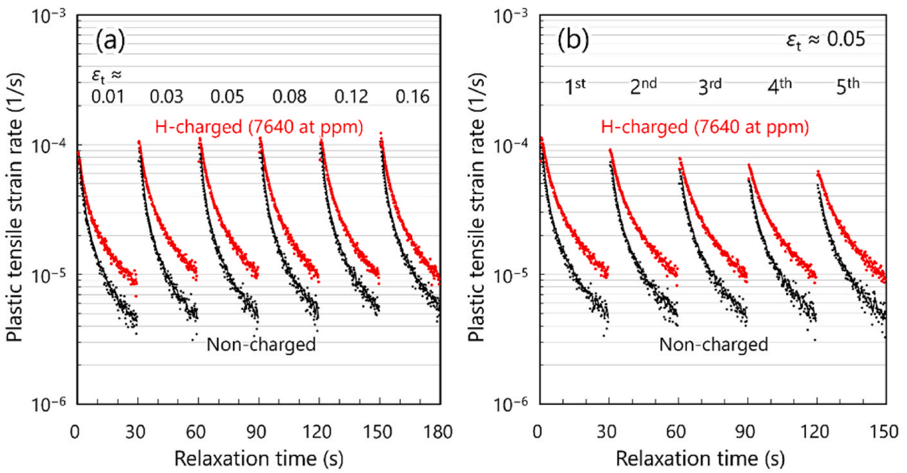

**Fig. 5.** Plastic strain rates in non-charged and H-charged (7640 at ppm) specimens during (a) the first relaxation of each relaxation series at various strain levels, as well as during (b) 1st~5th relaxations at the true tensile strain around 0.05. Note additionally that the strain rates implemented in the strain rate jump test were $10^{-4}$~$10^{-5}$/s.

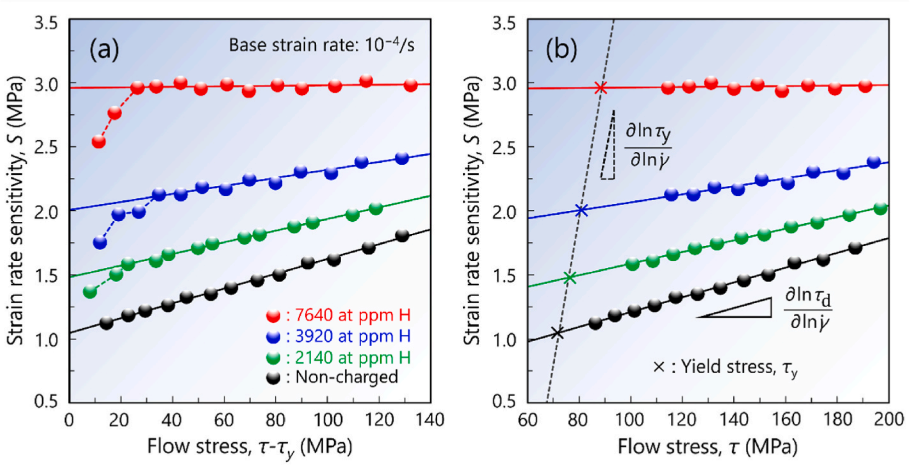

**Fig. 6.** Stress dependences of SRS (*i.e.*, Haasen plot), reproduced from Fig. 4 (b) using eqs. (3) and (8) of the specimens with various H concentrations measured in repeated stress relaxation tests at 296 K with the base strain rate of $10^{-4}$/s. The horizontal axis was taken as (a) $\tau-\tau_y$ and (b) $\tau$ in line with eq. (8a) and (8b), respectively. The raw data of these diagrams can be found in Appendix A4.

centration increased (Fig. 6 (a)). First, the overall SRS was increased by H, resembling the strain rate jump test (Fig. 3 (b)). Second, the SRS increased as a function of flow stress with a steeper slope at a low-stress ($\tau-\tau_y = \sim 30$ MPa), while the steep slope ceased, and almost linear plots were obtained after $\tau-\tau_y = 40$ MPa (true tensile strain around 0.03). We refer to this latter domain as a "steady state" regime. The slope in the steady state regime was gradually reduced with the increase in H concentration. Finally, the plot became almost horizontal at 7670 at ppm H. Back extrapolation of the steady-state regime resulted in positive intercepts with higher values than that in the non-charged specimen. In Fig. 6 (b), the same Haasen plots (only steady-state regime) are reproduced with the horizontal axis of $\tau$ (cf. eq. (8b)). The yield stresses are

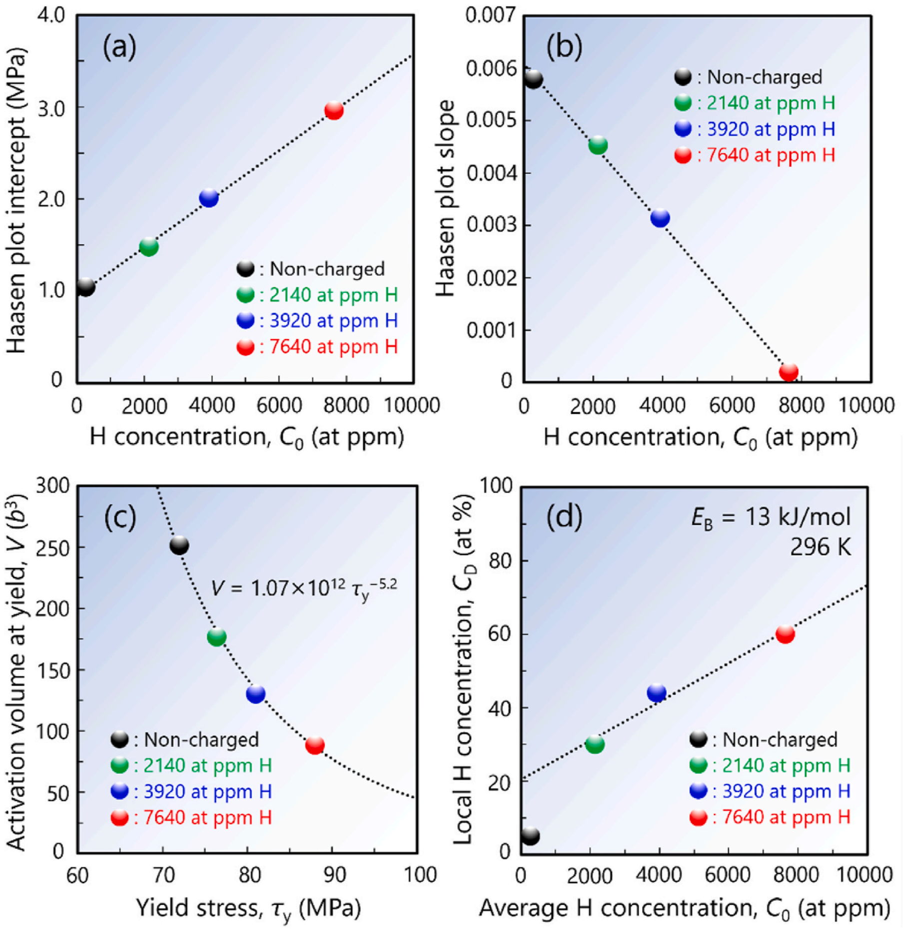

**Fig. 7.** (a) Intercepts and (b) slopes of the Haasen plot as a function of H concentration, extracted from Fig. 6. The intercepts were converted into activation volume *via* eq. (3) and plotted against yield stress in (c). (d) denotes local H concentrations in the near-dislocation core as a function of average H concentration (cf. eq. (11) in Section 5.3).

also marked in Fig. 6 (b) by crosses on the back extrapolation lines. A linear relationship, the slope of which corresponds to $\partial \ln \tau_y / \partial \ln \dot{\gamma}$ (see eq. (8b)), was found for the cross marks, indicating the proportionality between yield stress and the SRS at yielding.

Haasen plots were also obtained from strain rate jump tests (Fig. 3 (b)), and the data were almost consistent with stress relaxation tests (Appendix A5). Therefore, all the following descriptions and discussions are based only on stress relaxation tests. It is noteworthy that the two test methods led to an identical result.

The Haasen plot intercepts and slopes of the steady-state regime in Fig. 6 (a) are represented in Fig. 7 (a) and (b). There was an excellent positive linearity between the intercepts and H concentration, $C_0$. Combined with Fig. 6 (b) (*i.e.*, the proportionality of the SRS at yielding to the yield stress), this means that the yield stress was also proportional to $C_0$, reproducing the author's previous finding [3,17]. Also, the slope was a linearly decreasing function of $C_0$ (Fig. 7 (b)). The SRS at the Haasen plot intercepts were converted to $V$ by eq. (3) and plotted versus yield stress in Fig. 7 (c). A power law relationship between $V$ and $\tau_y$ was identified, and notably, both non-charged and H-charged specimens converged into one master curve.

## 5. Discussion

### 5.1. Key findings and the Haasen plot in the low-stress domain

Before attempting to revisit the H-dislocation interactions *via* Haasen plot, three key findings (Fig. 6) should be recalled again:

(i) Increase in SRS (decrease of activation volume) by solute H
(ii) Decrease in Haasen plot slope with increasing H concentration
(iii) The transition of Haasen plot from the low-stress domain with a steep slope to the high-stress (steady state) domain with a shallow slope (Fig. 6 (a))

The authors have investigated the influence of solute H on the stress-strain response of a Type310S steel and its dependence on strain rate and temperature [3]. At ambient temperature and strain rate of $10^{-5}\sim10^{-4}$/s, resistance force by dragging of H atmosphere on dislocations [63–65] could contribute to the flow stress at the strain below 0.1, accompanying a temporal decay of strain-hardening rate like Fig. 1 (b). Similarly, the transition of Haasen plot slope appeared around $\tau - \tau_y = 40$ MPa (Fig. 6 (a)), where the corresponding strain was ~0.03. Besides, the decrease of strain-hardening rate by H under the strain below 0.1 was evident as well in Fig. 1 (b). Thus, the low-stress domain might also be affected by an atmosphere drag force, overriding the intrinsic H-impact on thermally activated movement of dislocations. As the deformation progresses and $\rho_m$ increases, dislocation velocity falls below the limit of no drag force [64,65], at which H atmosphere can follow the dislocations by maintaining its equilibrium distribution. This could be reached when $\rho_m$ well exceeded $10^{13}$ 1/m$^2$ under a strain rate below $10^{-4}$ 1/s. Considering the theoretically calculated $\rho_m$ in FCC metals [66,67], $\rho_m > 10^{13}$ 1/m$^2$ is reasonable in the intermediate to later stages of plastic deformation (see Appendix A6). Additionally, Estrin and Kubin stated that the plastic deformation under small strain is highly heterogeneous [67], further complicating the interpretation through eqs. (1)-(10). For these reasons, we excluded the point (iii) from the present discussion framework. The primary focus was placed on the steady-state regime, where Haasen plot becomes linear, and the plasticity becomes more homogeneous [67]. One has to emphasize that the above results (i) and (ii) were obtained with no significant impact of H on the dislocation structures (Fig. 2). Moreover, the *in-situ* neutron diffraction experiment in our companion work demonstrated that solute H of 7640 at ppm did not change the dislocation density under a given strain [68]. This implies that the influences of H on the Haasen plot intercept and slope were mainly caused by some changes in the mobility of individual dislocations.

### 5.2. Increases in strain rate sensitivity and Haasen plot intercept

In the steady-state regime, solute H consistently increased the Haasen plot intercept (Fig. 6 (a)). A larger intercept indicates an increase in SRS due to the matrix frictional stress and, in turn, a decrease in the frictional component of activation volume (eqs. (8) and (9)) [43,45,48]. The linear superposition law of flow stress (*i.e.*, a rationale of eqs. (8) and (9)) is valid only when the dispersion interspacing of each kind of obstacle contributing to $\tau_y$ and $\tau_d$ is more than an order of magnitude different from the other [48,57]. Under such a situation, the resistance by higher-density obstacles can be considered as background friction, simply overriding the resistance by more coarsely spaced second-type obstacles. Given that the average planar interspacing of H atoms, $L_H$, is $b/C_0^{1/2}$ [69] or $(3^{1/2}b^2/4C_0)^{1/2}$ [70], 2000–7600 at ppm yields $L_H =$ 2–5 nm. Meanwhile, the forest dislocation (*i.e.*, obstacles responsible for $\tau_d$) interspacing, $L_d$, can roughly be estimated by eq. (10). Within the present flow stress range (10–130 MPa (Fig. 6 (a)), $L_d$ is ≈ 80–1000 nm. This large gap between $L_H$ and $L_d$ validates the applicability of linear superposition law for solute H and forest dislocations. Furthermore, the interspacing of H atoms near the dislocation line could even be smaller, as discussed below (Section 5.3.1).

The superposition law of solute H and forest dislocation effects is further valid if one compares Haasen plots under 2000–4000 at ppm H with that of the non-charged sample. An increase in the intercept caused an upward shift of Haasen plots, while the change of their slope was minor (Fig. 6). It is a well-established tenet that the increase in Haasen plot intercept reflects the involvement of additional short-range obstacles, the density of which is independent of strain [43–45,48,71]. Ultimately, the greater intercept in the H-charged specimens reaches the most important statement in the present paper: *whatever the underlying mechanisms, H atoms function as newly involved weak (i.e., more localized and thermally activatable) obstacles, hindering the movement of dislocations rather than enhancing it.* This conclusion supports some claims in the recent experiments [15,17] and atomistic simulations [13,14]. Although the latter simulations [13,14] were performed on BCC iron, more effective obstruction of dislocation motion can be anticipated in FCC due to its much higher solute H concentration. *Under a faster strain rate where energy supplied by thermal vibration is statistically reduced* (cf. *eq. (1b)), the dislocations experience more resistance from these weaker obstacles, while much lower stress is required to overcome these weak obstacles when the strain rate is low.* This is a rationale for the increasing SRS by solute H. In this context, an enhancement of stress relaxation by H under a fixed strain (Fig. 3 (a)) [2,16] is now interpreted from a completely different viewpoint. That is, *an overridden thermal stress due to solute H themselves is relaxed as the dislocations get more chance to overcome H atoms with the aid of time.* The longer creep duration under fixed stress [1] is similarly understood as the delay of deformation by the involvement of such an additional kind of short-range obstacles. Ultimately, Fig. 6 gives us a revision of the past brief on the dual roles of solute H: enhancement of slow dislocation movement; retardation of rapid dislocation movement [1,2,16]. The origin of the superficial softening, which has been observed in previous stress relaxation and creep tests, is now clarified.

### 5.3. Model of H-dislocation interaction

#### 5.3.1. Basic features

When the $V$ at yield stress was measured from the Haasen plot intercept, there was a power law relationship between $V$ and $\tau_y$ (Fig. 7 (c)). Non-charged and H-charged specimens converged into one master curve, a phenomenon called "stress equivalence": yield stress is solely correlated with $V$ irrespective of solute species and concentration [70, 72–74]. Nonetheless, the power law exponent of −5.2 was somewhat larger than previously reported values, *e.g.*, −2/3 [75]. This is possibly due to the specific process of the thermal activation event discussed below.

In an attempt to model H-dislocation interactions, a noteworthy point of stress-equivalence is that we can treat solute H on a comparable basis with other alloying elements rather than accounting for it as a special element. To rationalize the stress-equivalent nature of $V$, Basinski et al. pointed out the simultaneous participation of multiple solute atoms in an elemental thermal activation event [70]. In our present case, the plausible $V$ for a single H atom should be around $10b^3$, if H is assumed as a point-like obstacle, and their mean interspacing, $L_H$, and effective width, $d$, are approximated as $L_H \approx (3^{1/2}b^2/4C_0)^{1/2}$ and $d \approx b$. This is indeed an order of magnitude smaller than our experimental results (Fig. 4 (b)). Also, such $L_H$ underestimates the H density close to the dislocation core since it neglects the local segregation of H atoms and their coordinative motion with moving dislocations (Appendix A6).

Kocks [73], as well as Butt and Feltham [74], proposed a *trough model* of solution-hardening, wherein multiple solute atoms are involved in each thermal activation process. In their assumption, a dislocation line initially lays along a row of solutes, a potential well reducing the dislocation's line tension. The dislocation then surmounts the energy trough (*i.e.*, local pinning by a solute row) *via* bowing-out a short segment with the help of applied stress and thermal vibration. The solutes contributing to such an event may be randomly dispersed ones or those dynamically segregating to the dislocation by diffusion [73]. Notably, the line energy reduction assumed in their model resembles the thermo-mechanical H-dislocation interaction theory developed by Kirchheim [76,77]. Whatever the type of solutes, the reduction in line tension, *i.e.*, a sole parameter determining $V$ and $\Delta G$, relies on the interaction force of the dislocation with the solutes per its unit length [73]. This one-parameter description of $\Delta G$ constitutes the backbone of stress equivalence in solution-hardened alloys [70,72]. Another essential consequence of the trough model is the proportionality of $1/\Delta G$ and $1/V$ (SRS) with stress. In fact, such a linear correlation between SRS and stress is obeyed in Fig. 6 (b).

Assuming a near-equilibrium state of H distribution in the proximity of mobile dislocation, the local H concentration close to the dislocation core, $C_D$, is estimated by Fermi-Dirac statistics [78].

$$\frac{C_D}{1-C_D}=\frac{C_0}{1-C_0}\exp\left(\frac{E_B}{RT}\right) \tag{11}$$

where $R$ is gas constant, $T$ is temperature, and $E_B$ is the binding energy between the dislocation core and solute H: ≈13 kJ/mol has been reported for austenitic steels [79–81]. In Fig. 7 (d), the $C_D$ at 296 K, which were estimated by eq. (11), are plotted versus $C_0$. Except for the non-charged specimen, $C_0$ is almost proportional to $C_D$ within the present H concentration range of 2140~7640 at ppm. If the linear H density along the dislocation line is also proportional to $C_D$, and the bulging simply follows the general breakaway process from a stationary solute atmosphere [82], the critical bow-out length, $l_c$, is a reciprocal function of $C_D$ ($l_c \sim 1/C_D$) [69]. Given that the forward bow-out displacement is small compared with $l_c$, $1/V$ is proportional to $C_0$ and $C_D$. On this presumption, a linear increase of yield stress with increasing $C_0$ (*i.e.*, ≈80 MPa/at% H [17]) seems to be plausible. Imagining an even greater $C_0$, $C_D$ should eventually saturate (eq. (11)), and the effectiveness of $C_0$ to decrease the $V$ and increase the yield stress would cease (*i.e.*, the linearity between $C_0$ and $C_D$ in Fig. 7 (d) would break down). Indeed, a non-linear and more logarithmic increase of yield stress with increasing $C_0$ was reported by Abraham and Altstetter, when $C_0$ was higher than a few at% [31]. The tentative model of H-dislocation interaction responsible for increasing thermal stress and decreasing $V$ is schematically drawn in Fig. 8 for low and high H concentrations. In the next section, the movement of H atoms near the dislocation core with the forward dislocation motion (indicated by dilute red circles in Fig. 8) will be further taken into account. Meanwhile, the H concentration near the dislocation core is much smaller in the non-charged specimen as compared with H-charged specimens (Fig. 7 (d)). Under such a circumstance, denser alloying elements, including Cr and Ni, predominate the thermal activation event instead, giving rise to the $V$ that is still stress-equivalent with the H-charged specimens (Fig. 7 (c)).

### 5.3.2. *Dislocation glide controlled by H-diffusion*

An assignment for establishing the H-dislocation interaction model is to consider how a core H atom behaves as an effective obstacle. The dislocation pinning by segregated H atoms is likely when the diffusion of H is slow compared with the dislocation velocity [4,83]. However, in the present situation, migration of the H atmosphere is comparable with dislocation movement, wherein the dislocation pinning effect by segregated solutes becomes questionable in general [42,69]. As such, we have to postulate some specific forms of H-dislocation interactions, which restrict the coordinative motion of H with dislocations. Or else, some trap sites should exist that immobilize the H atoms near the dislocation core, even though the migration of the whole H atmosphere is still fast enough.

The solute drag theory in Refs. [64,65] (Appendix A6) only considers the remote interaction between a dislocation and solutes, excluding any phenomena locally occurring in the dislocation core region. Outside the cutoff radius of $\approx 2b$ from the dislocation center, the migration of solutes with a moving dislocation is rather faster than that expected from bulk diffusivity: the chemical potential gradient and attractive force from the dislocation enhances the solute flux [42,65]. In fact, if the dislocation velocity, $v_d$, at $\rho_m = 10^{13}$ 1/m$^2$ [66] and $\dot{\varepsilon_{Pl}} = 10^{-4}$/s was estimated by the Orowan equation: $\dot{\varepsilon_{Pl}} = \rho_m b v_d / M$ [25], one obtains $v_d \approx 10^{-7}$ m/s. This is an order of magnitude greater than the migration distance of H through the matrix when the calculation is done by $(Dt)^{1/2}$ ($D = 3.2 \times 10^{-16}$ m$^2$/s at 296 K (Appendix A6)). However, for an unsaturated atmosphere with $E_B > kT$, the follow-up of the solutes in the dislocation core is directly linked to the bulk diffusion activation energy of solutes. This situation is the so-called *diffusion-controlled glide* [42], wherein the resistance force against dislocation motion emerges even when the long-range drag force is trivial. The problem was solved by Friedel, who formulated the corresponding resistance stress, $\sigma_{mc}$, under a given strain rate on the assumption that the average spacing between each solute atom along the dislocation core is $b/C_D$ [84]:

$$\sigma_{mc}=\frac{kT}{b^3C_D}\sinh^{-1}\left(\frac{C_D\dot{\varepsilon_{pl}}}{2\rho_m D}\right) \tag{12}$$

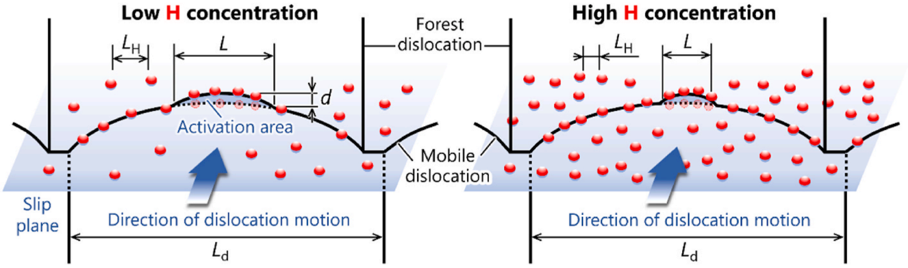

**Fig. 8.** Schematic drawing of a model for the thermal stress escalation and activation volume reduction *via* H-dislocation interactions at low and high H concentrations. The dislocation moves by bowing out its short segment from the energy trough of a linear array of segregated H, where critical bow-out length is determined by the linear density of H along the dislocation line.

Adopting $\rho_m = 10^{13}$ 1/m$^2$, $C_D = 60\%$ (Fig. 7 (d)), $\dot{\varepsilon}_{Pl} = 10^{-4}$/s, and $D = 3.2 \times 10^{-16}$ m$^2$/s, we obtain a sizeable value of 1.5 MPa. One of the reasons for this smaller value than the magnitude of practical stress relaxation (Fig. 4 (a)) is that eq. (12) only considers a jump of a single H atom, while multiple H atoms might simultaneously contribute to a unit activation event (Section 5.3.1). Moreover, as described below, there would be some additional contributions from the interactions between H and substitutional solutes. The dislocation bow-out (Fig. 8) potentially progresses where the collective jump of H atoms in the dislocation core incidentally happens.

### *5.3.3. Potential role of H-substitutional interaction*

The influence of alloy composition on the H absorption capacity and solution-hardenability in Fe–Cr–Ni system was investigated by the authors, identifying a greater H solubility and strengthening with increasing Cr content [17]. Moriyama et al. verified this effect of Cr using first-principles calculations [85]. They demonstrated more than 10 kJ/mol decrease of the H absorption energy in the O-sites surrounded by two peripheral Cr atoms in comparison to others consisting only of Fe or Fe–Ni. A high chemical affinity between H and Cr has been reported similarly in several other previous studies [86,87]. The activation energy for bulk H diffusion in austenite is ≈ 50 kJ/mol [62,88]. Nevertheless, once an H atom sinks into Cr-rich O-sites, it may be temporarily trapped because an extra energy corresponding to Cr–H binding is required to jump into neighboring O-sites. The significance of such Cr–H interaction may not appear in the traditional H diffusion data of austenitic steels since the experimental difficulty restricted the diffusivity measurement at hundreds of centigrade [62,88], where the influence of local trapping might become negligible. If segregated H atoms form Cr–H complexes in the dislocation core, the attractive interaction between Cr and H counteracts the driving force of dislocation to drag the H. This possibly exerts a resistance against dislocation motion through the process described in Section 5.3.2. The validity of the present diffusion-controlled glide model and the importance of Cr–H complexes can be supported by the disappearance of the H-induced increase in flow stress around 400 K [3]. At an elevated temperature, the Cr–H binding could no longer be stable, and the jump of H atoms near the dislocation core is readily so fast that the resistance stress defined by eq. (12) becomes negligible.

In the author's experiments that examined the strain rate effects on the H-induced solution-hardening, an H-induced increase in flow stress was, however, still observed under a fast strain rate ($5 \times 10^{-3}$/s), wherein the coordinative motion of H with dislocations was infeasible [3]. Thus, Cr–H complexes randomly dispersed through the matrix also act as short-range obstacles when they incidentally encounter moving dislocations. In Fe–Cr–Ni-based austenitic steels, an H-induced Snoek peak was reported in internal friction measurements [87,89,90]. The peak was attributed to the tetragonal distortion owing to H-substitutional complexes [90]. These tetragonal obstacles strongly interact with dislocations, as for the interstitials in the BCC lattice [69], further rendering the dispersed Cr–H complexes as dislocation pinning points.

## *5.4. Decrease in Haasen plot slope*

The slope of Haasen plot, governed by interactions between dislocations (eq. (8)), was decreased by H and became almost zero at the concentration of 7640 at ppm (Fig. 6). Similar slope change has been discussed in various conventional solution-strengthened alloys. In fact, most of the solute species, not only H, consistently tend to decrease the slope [43,45,46].

According to the description by Mulford, the slope of Haasen plot is inversely proportional to the work required for a mobile dislocation to penetrate through a forest dislocation [43]. One possible reason for such an obstruction effect is a reduction in stacking fault energy (SFE), *i.e.*, extra work to constrict the two extended Shockley partials [25] before intersecting with forests, seeming reasonable since H in austenitic steels has been believed to decrease SFE [81,91]. Nevertheless, some inevitable consequences from the decrease in SFE must also be regarded: strain-hardening, especially the critical stress and strain for dynamic recovery, should be increased [92,93]. In the author's previous investigation, no significant change in the onset of dynamic recovery was found in Fe–Cr–Ni austenitic steels after H-charging [17]. Furthermore, our companion work using *in-situ* neutron diffraction experiments detected almost no H-effect on the probability of stacking fault under the H concentration of 7640 at ppm [68]. As such, only the decrease of SFE can, if any, not rationalize the decrease in Haasen plot slope under the presence of H.

A different approach to the solute-induced decrease in Haasen plot slope was attempted by Curtin [45] and Niewczas et al. [46] on the assumption that, when the solutes are more rate-sensitive than forest dislocations, $\Delta G$ is governed by the former. The hypothesis by Curtin led to

$$S = \frac{kT}{V} = \frac{kT}{V_S} + \frac{kT}{V_S}\frac{1}{\tau_S}(\tau - \tau_S) \tag{13}$$

in which the Haasen plot slope is $(kT/V_S)/(1/\tau_S)$. Here, subscript S means the component stemming only from the solutes. The $kT/V_S$ is approximated by the Haasen plot intercepts. Besides, $\tau_S$ can roughly be taken as yield stress, although strengthening by grain boundaries has some contributions of a few tens of MPa under a grain size of 30∼70 μm [94]. Plugging into these values, the slope is an order of $10^{-2}$, which is obviously larger than our experimental measurements (Fig. 7 (b)). The predominance of solute atoms rather than forest dislocations in determining the Haasen plot behavior [45,46] may rationalize the tendency found in Fig. 6 to some extent. Nevertheless, eq. (13) alone cannot quantitatively account for the extremely small Haasen plot slope at the H concentration of 7640 at ppm. On the contrary, the line tension model of dislocation movement through a field of different obstacle types predicted that the overall activation energy and SRS are predominated by stronger obstacles rather than weaker ones [95,96]. However, since it is unlikely that the obstruction by H, a quite small interstitial, is stronger than dislocation-dislocation intersections, the insusceptibility of SRS to stress/strain under the presence of H is not rationalized, no less.

The change of Haasen plot slope in solution-hardened alloys has often been attributed to solute diffusion (*i.e.*, dynamic strain aging (DSA)) [47,48,52,73]. Under a fixed chemical composition of the alloy, it was identified that only the slope decreased with the increase in temperature, while the intercept remained constant [47,48]. Diffusing solutes may strengthen dislocation junctions or re-lock mobile dislocations by segregating their vicinity during the waiting time of mobile dislocations at the intersecting forests [47,52,97]. The waiting time and the number of strengthened junctions are both the direct functions of dislocation density [52,97], a controlling factor for the strain-hardening component of activation volume and SRS (eq. (8)-(10)). Because of this time-dependent decrease in the dislocation mobility, $S_d$ in eq. (8a) decreases and eventually becomes negative. Notwithstanding, additional segregation of H is not anticipated in the present deformation condition, where H always forms an almost equilibrium atmosphere around dislocations (Appendix A6). Moreover, there is no premise that H strengthens dislocation junctions, whereas H may conversely weaken the junctions somehow [98,99].

One plausible mechanism, which is related to dislocation density, is the creation of vacancies and their clusters through dislocation motion. Owing to the jog formation *via* screw dislocations cutting, subsequent jog-dragging, or pinching off of dipolar segments after cross-slip, rows of vacancies or vacancy-type prismatic dislocation loops are formed [25,100,101]. These loops readily act as debris, obstructing the movement of dislocations [100]. The importance of strain-induced vacancies is established in the DSA of austenitic steels as their paring with interstitial carbon [102]. In a similar manner, their significance should become more intense in H-charged materials in view that H atoms trapped in vacancies stabilize them and, thereby, increase their density [103,104]. Hatano et al. [105] and Fujinami et al. [106,107] provided evidence for the higher density of strain-induced vacancies and vacancy clusters in H-charged austenitic steels *via* positron annihilation spectroscopy measurements. The role of these H-vacancy complexes to obstruct the dislocation movement was experimentally [108] and analytically [109] confirmed, in which the obstruction effect increases as the number of absorbed H atoms in a vacancy and the cluster size increase. Indeed, recent crystal plasticity modeling successfully reproduced the experimentally obtained stress-strain curve of H-charged austenitic steel by taking into account the role of H-vacancy complexes [110]. Depending on the material type, the binding energy between H atoms and a vacancy is maximized when certain numbers of H atoms are involved [111–114]. Attainment of such an energetically favorable configuration, as well as the clustering of vacancies, would be time-consuming processes [115] since there is no remote interaction between a vacancy and nearby H [112]. In addition, the trapped H atoms slow down the diffusion of vacancies themselves [116]. Meanwhile, the H-vacancy complexes gradually become unstable if more H atoms than the lowest energy state are incorporated [111,113,114]. Thus, given that the statistical form defined by eq. (11) is applicable, the concentration of vacancies associated with a larger number of H atoms increases with $C_0$ [117]. As the mobile and forest dislocations multiply, the row of vacancies left behind jogs are created one after another. These vacancies arrange themselves into H-involving clusters, a process that is diffusion-controlled and acts as an effective barrier to dislocation motion. Under a greater $C_0$, it is likely that the clusters consisting of a greater number of vacancies and containing a larger number of H (*i.e.*, obstacles stronger than those with fewer H) increase. The interactions of mobile dislocations with those large vacancy clusters [109], which might be more rate-insensitive, possibly compensated the SRS component stemming from the ordinary interactions between mobile and forest dislocations.

## 6. Conclusions

The influence of solute hydrogen (H) on thermally activated deformation of Type310S austenitic steel was studied primarily by stress relaxation tests at 296 K. Bulk specimens with a 6 mm diameter were uniformly pre-charged with ~7600 at ppm H in a gaseous $H_2$ environment. Elaborating on these transient mechanical tests using *Haasen plot* (*i.e.*, strain-rate sensitivity (SRS) vs. flow stress), we reached the following main conclusions.

1. The effect of solute H on thermally activated deformation was characterized by three primary aspects: enhancement of stress relaxation, reduction in activation volume, and increase in SRS. These are mutually the same in their physical meaning and phenomenologically coincident with the past experimental findings.
2. The Haasen plot indicated an increase in frictional stress component by solute H. H atoms acted as weak, short-range obstacles, which were more thermally activatable than other intrinsic obstacles involved in the material. *The net effect of solute H is to invariably retard thermally activated movement of dislocations*, whatever the underlying mechanisms are. Such a contribution of an additional type of thermal obstacle (*i.e.*, an increase in thermal stress component) is a central reason for the increase of flow stress (*i.e.*, solid-solution hardening) on the stress-strain curve of H-charged samples.
3. The thermal activation process of a dislocation to overcome solute H was stress-equivalent, where one-to-one correspondence exists between activation volume, $V$, and yield stress, $\tau_y$: $V \propto \tau_y^{-5.2}$. The stress-equivalence also led to a proportionality between the SRS at yielding and the H concentration. According to these facts, the model of H-dislocation interaction (Fig. 8) was proposed, where a dislocation segment bow-out from the row of segregated H atoms with the aid of thermal vibration. The model can rationalize the linear correlation between the yield stress and H concentration (*i.e.*, ≈80 MPa/at% H) found in our previous work.

## CRediT authorship contribution statement

**Yuhei Ogawa:** Writing – original draft, Investigation, Funding acquisition, Conceptualization. **Masaki Tanaka:** Writing – review & editing, Validation, Conceptualization. **Takeshi Fujita:** Investigation, Data curation. **Akinobu Shibata:** Writing – review & editing, Supervision.

## Declaration of competing interest

The authors declare that they have no known competing financial interests or personal relationships that could have appeared to influence the work reported in this paper.

## Acknowledgments

This work was supported by research funding from JSPS KAKENHI (Grant Number: 21K14045), JFE 21st CenturyFoundation, and The Iwatani Naoji Foundation, as well as by NIMS microstructural characterization platform as a program of “Nanotechnology Platform” of the Ministry of Education, Culture, Sports, Science and Technology (MEXT), Japan, Grant Number JPMXP1223NM5395. The authors' series of studies regarding the H-effects on mechanical properties of austenitic steels originated from the research framework funded by the Japan Science and Technology Agency (JST) (grant: #20100113, FY2014~FY2019) under the Industry-Academia Collaborative R&D Program “Heterogeneous Structure Control” (P.O.: Late Professor Masaharu Kato). All of the mechanical tests and hydrogen-charging in this study were performed during Y.O.‘s tenure at Kyushu University, where he was affiliated until February 2023 (currently affiliated with NIMS). Y.O. and T.F. are grateful to the members of the Research Center for Hydrogen Industrial Use and Storage (HYDROGENIUS), Kyushu University, for their provision of research facilities and support in hydrogen charging. Y.O. also expresses his gratitude to Prof. Kenji Higashida from Kyushu University and Prof. Kaneaki Tsuzaki from NIMS for their fruitful expertise and discussion.

## Appendix A. Supplementary data

Supplementary data to this article can be found online at https://doi.org/10.1016/j.ijhydene.2024.06.113.

## References

[1] Tien CW, Altstetter CJ. Hydrogen-enhanced plasticity of 310S stainless steel. Mater Chem Phys 1993;35:58–63. https://doi.org/10.1016/0254-0584(93)90177-N.

[2] Abraham DP, Altstetter CJ. Hydrogen-enhanced localization of plasticity in an austenitic stainless steel. Metall Mater Trans 1995;26:2859–71. https://doi.org/10.1007/BF02669644.

[3] Ogawa Y, Takakuwa O, Tsuzaki K. Solid-solution hardening by hydrogen in Fe–Cr–Ni-based austenitic steel: temperature and strain rate effects. Mater Sci Eng 2023;879:145281. https://doi.org/10.1016/j.msea.2023.145281.

[4] Boniszewski T, Smith GC. The influence of hydrogen on the plastic deformation ductility, and fracture of nickel in tension. Acta Metall 1963;11:165–78. https://doi.org/10.1016/0001-6160(63)90209-8.

[5] Blakemore JS. The portevin-le chatelier effect in hydrogenated nickel alloys. Metall Mater Trans 1970;1:151–6. https://doi.org/10.1007/BF02819255.

[6] Asano S, Otsuka R. The lattice hardening due to dissolved hydrogen in iron and steel. Scripta Metall 1976;10:1015–20. https://doi.org/10.1016/0036-9748(76)90119-8.

[7] Matsui H, Kimura H, Moriya S. The effect of hydrogen on the mechanical properties of high purity iron I. Softening and hardening of high purity iron by hydrogen charging during tensile deformation. Mater Sci Eng 1979;40:207–16. https://doi.org/10.1016/0025-5416(79)90191-5.

[8] Beachem CD. A new model for hydrogen-assisted cracking (hydrogen “embrittlement”). Metall Trans A 1972;3:441–55. https://doi.org/10.1007/BF02642048.

[9] Tabata T, Birnbaum HK. Direct observations of the effect of hydrogen on the behavior of dislocations in iron. Scripta Metall 1983;17:947–50. https://doi.org/10.1016/0036-9748(83)90268-5.

[10] Matsumoto T, Eastman J, Birnbaum HK. Direct observations of enhanced dislocation mobility due to hydrogen. Scripta Metall 1981;15:1033–7. https://doi.org/10.1016/0036-9748(81)90249-0.

[11] Birnbaum HK, Sofronis P. Hydrogen-enhanced localized plasticity—a mechanism for hydrogen-related fracture. Mater Sci Eng 1994;176:191–202. https://doi.org/10.1016/0921-5093(94)90975-X.

[12] Kirchheim R. Solid solution softening and hardening by mobile solute atoms with special focus on hydrogen. Scripta Mater 2012;67:767–70. https://doi.org/10.1016/j.scriptamat.2012.07.022.

[13] Song J, Curtin WA. Mechanisms of hydrogen-enhanced localized plasticity: an atomistic study using α-Fe as a model system. Acta Mater 2014;68:61–9. https://doi.org/10.1016/j.actamat.2014.01.008.

[14] Matsumoto R, Oyinbo ST, Vijendran M, Taketomi S. Hydrogen effect on the mobility of edge dislocation in α-iron: a long-timescale molecular dynamics simulation. ISIJ Int 2022;62. https://doi.org/10.2355/isijinternational.ISIJINT-2022-311. ISIJINT-2022-311.

[15] Koyama M, Ichii K, Tsuzaki K. Strain rate and temperature effects on hydrogen embrittlement of stable and metastable high-entropy alloys. Phys Mesomech 2022;25:385–92. https://doi.org/10.1134/S1029959922050010.

[16] Ogawa Y, Hosoi H, Tsuzaki K, Redarce T, Takakuwa O, Matsunaga H. Hydrogen, as an alloying element, enables a greater strength-ductility balance in an Fe-Cr-Ni-based, stable austenitic stainless steel. Acta Mater 2020;199:181–92. https://doi.org/10.1016/j.actamat.2020.08.024.

[17] Nishida H, Ogawa Y, Tsuzaki K. Chemical composition dependence of the strength and ductility enhancement by solute hydrogen in Fe–Cr–Ni-based austenitic alloys. Mater Sci Eng 2022;836:142681. https://doi.org/10.1016/j.msea.2022.142681.

[18] Bernstein IM. The effect of hydrogen on the deformation of iron. Scripta Metall 1974;8:343–9. https://doi.org/10.1016/0036-9748(74)90136-7.

[19] Moriya S, Matsui H, Kimura H. The effect of hydrogen on the mechanical properties of high purity iron II. Effect of quenched-in hydrogen below room temperature. Mater Sci Eng 1979;40:217–25. https://doi.org/10.1016/0025-5416(79)90192-7.

[20] Matsui H, Kimura H, Kimura A. The effect of hydrogen on the mechanical properties of high purity iron III. The dependence of softening in specimen size and charging current density. Mater Sci Eng 1979;40:227–34. https://doi.org/10.1016/0025-5416(79)90193-9.

[21] Kimura A, Matsui H, Kimura H. The work-hardening behaviour of hydrogen-charged high purity iron single crystals at temperatures between 296 and 200 K. Mater Sci Eng 1983;58:211–22. https://doi.org/10.1016/0025-5416(83)90047-2.

[22] Park CG, Shin KS, Nagakawa J, Meshii M. Effect of cathodic charging on creep and tensile deformation of pure iron. Scripta Metall 1980;14:279–84. https://doi.org/10.1016/0036-9748(80)90109-X.

[23] Oguri K, Kimura H. The effect of hydrogen on the flow stress of iron with various purities. Scripta Metall 1980;14:1017–22. https://doi.org/10.1016/0036-9748(80)90378-6.

[24] Wang S, Hashimoto N, Wang Y, Ohnuki S. Activation volume and density of mobile dislocations in hydrogen-charged iron. Acta Mater 2013;61:4734–42. https://doi.org/10.1016/j.actamat.2013.05.007.

[25] Hull D, Bacon DJ. Introduction to dislocations. third ed. Butterworth-Heinemann; 2011. https://doi.org/10.1016/C2009-0-64358-0.

[26] Sun Q, He J, Nagao A, Ni Y, Wang S. Hydrogen-prompted heterogeneous development of dislocation structure in Ni. Acta Mater 2023;246:118660. https://doi.org/10.1016/j.actamat.2022.118660.

[27] Yamabe J, Wada K, Awane T, Matsunaga H. Hydrogen distribution of hydrogen-charged nickel analyzed via hardness test and secondary ion mass spectrometry. Int J Hydrogen Energy 2020;45:9188–99. https://doi.org/10.1016/j.ijhydene.2020.01.117.

[28] Wada K, Yamabe J, Ogawa Y, Takakuwa O, Iijima T, Matsunaga H. Comparative study of hydrogen-induced intergranular fracture behavior in Ni and Cu–Ni alloy at ambient and cryogenic temperatures. Mater Sci Eng 2019;766:138349. https://doi.org/10.1016/j.msea.2019.138349.

[29] Symons DM. Hydrogen embrittlement of Ni-Cr-Fe alloys. Metall Mater Trans 1997;28:655–63. https://doi.org/10.1007/s11661-997-0051-4.

[30] Wada K, Yamabe J. The effect of the Ni/Cu ratio on H-induced ductility loss and its mechanism in Cu–Ni binary alloy system. Int J Hydrogen Energy 2021;46:39577–89. https://doi.org/10.1016/j.ijhydene.2021.09.140.

[31] Abraham DP, Altstetter CJ. The effect of hydrogen on the yield and flow stress of an austenitic stainless steel. Metall Mater Trans 1995;26:2849–58. https://doi.org/10.1007/BF02669643.

[32] San Marchi C, Somerday BP, Tang X, Schiroky GH. Effects of alloy composition and strain hardening on tensile fracture of hydrogen-precharged type 316 stainless steels. Int J Hydrogen Energy 2008;33:889–904. https://doi.org/10.1016/j.ijhydene.2007.10.046.

[33] Yamabe J, Takakuwa O, Matsunaga H, Itoga H, Matsuoka S. Hydrogen diffusivity and tensile-ductility loss of solution-treated austenitic stainless steels with external and internal hydrogen. Int J Hydrogen Energy 2017;42:13289–99. https://doi.org/10.1016/j.ijhydene.2017.04.055.

[34] Takakuwa O, Mano Y, Soyama H. Increase in the local yield stress near surface of austenitic stainless steel due to invasion by hydrogen. Int J Hydrogen Energy 2014;39:6095–103. https://doi.org/10.1016/j.ijhydene.2014.01.190.

[35] Chateau JP, Delafosse D, Magnin T. Numerical simulations of hydrogen–dislocation interactions in fcc stainless steels.: part I: hydrogen–dislocation interactions in bulk crystals. Acta Mater 2002;50:1507–22. https://doi.org/10.1016/S1359-6454(02)00008-3.

[36] Ferreira PJ, Robertson IM, Birnbaum HK. Hydrogen effects on the interaction between dislocations. Acta Mater 1998;46:1749–57. https://doi.org/10.1016/S1359-6454(97)00349-2.

[37] Lu G, Zhang Q, Kioussis N, Kaxiras E. Hydrogen-enhanced local plasticity in aluminum: an ab initio study. Phys Rev Lett 2001;87:095501. https://doi.org/10.1103/PhysRevLett.87.095501.

[38] Wang S, Nagao A, Edalati K, Horita Z, Robertson IM. Influence of hydrogen on dislocation self-organization in Ni. Acta Mater 2017;135:96–102. https://doi.org/10.1016/j.actamat.2017.05.073.

[39] Tabata T. Direct observation of the effect of hydrogen on the mechanical properties of iron. Bull Jpn Inst Met 1985;24:485–93. https://doi.org/10.2320/materia1962.24.485.

[40] Matsumoto R, Taketomi S. Molecular dynamics simulation of Surface-Adsorbed-Hydrogen-Induced Dislocation Motion in a thin film. Comput Mater Sci 2020;171:109240. https://doi.org/10.1016/j.commatsci.2019.109240.

[41] Sirois E, Birnbaum HK. Effects of hydrogen and carbon on thermally activated deformation in nickel. Acta Metall Mater 1992;40:1377–85. https://doi.org/10.1016/0956-7151(92)90438-K.

[42] Caillard D, Martin JL. Thermally activated mechanisms in crystal plasticity. first ed. Pergamon; 2003.

[43] Mulford RA. Analysis of strengthening mechanisms in alloys by means of thermal-activation theory. Acta Metall 1979;27:1115–24. https://doi.org/10.1016/0001-6160(79)90129-9.

[44] Kocks UF, Chen SR. On the two distinct effects of thermal activation on plasticity: application to nickel. Phys Status Solidi 1992;131:403–13. https://doi.org/10.1002/pssa.2211310214.

[45] Curtin WA. New interpretation of the Haasen plot for solute-strengthened alloys. Scripta Mater 2010;63:917–20. https://doi.org/10.1016/j.scriptamat.2010.07.003.

[46] Niewczas M, Jobba M, Mishra RK. Thermally activated flow of dislocations in Al–Mg binary alloys. Acta Mater 2015;83:372–82. https://doi.org/10.1016/j.actamat.2014.09.056.

[47] Mulford RA, Kocks UF. New observations on the mechanisms of dynamic strain aging and of jerky flow. Acta Metall 1979;27:1125–34. https://doi.org/10.1016/0001-6160(79)90130-5.

[48] Kocks UF. Superposition of alloy hardening, strain hardening, and dynamic recovery. In: Strength of metals and alloys. Elsevier; 1979. p. 1661–80. https://doi.org/10.1016/B978-1-4832-8412-5.50250-2.

[49] Mecking H, Kocks UF. Kinetics of flow and strain-hardening. Acta Metall 1981;29:1865–75. https://doi.org/10.1016/0001-6160(81)90112-7.

[50] Haasen P. Plastic deformation of nickel single crystals at low temperatures. Phil Mag 1958;3:384–418. https://doi.org/10.1080/14786435808236826.

[51] del Valle JA, Picasso AC, Romero R. The superposition of flow stress contributions in a precipitate hardened Ni-based alloy studied by strain rate sensitivity measurements. Acta Mater 2003;51:6443–52. https://doi.org/10.1016/j.actamat.2003.08.014.

[52] Van Den Beukel A, Kocks UF. The strain dependence of static and dynamic strain-aging. Acta Metall 1982;30:1027–34. https://doi.org/10.1016/0001-6160(82)90211-5.

[53] Evans AG, Rawlings RD. The thermally activated deformation of crystalline materials. Phys Status Solidi 1969;34:9–31. https://doi.org/10.1002/pssb.19690340102.

[54] Groh P, Conte R. Stress relaxation and creep in α-iron filamentary single crystals at low temperature. Acta Metall 1971;19:895–902. https://doi.org/10.1016/0001-6160(71)90082-4.

[55] Martin JL, Kruml T. Characterizing thermally activated dislocation mobility. J Alloys Compd 2004;378:2–12. https://doi.org/10.1016/j.jallcom.2003.10.063.

[56] Spätig P, Bonneville J, Martin J-L. A new method for activation volume measurements: application to Ni3(Al,Hf). Mater Sci Eng 1993;167:73–9. https://doi.org/10.1016/0921-5093(93)90339-G.

[57] Dong Y, Nogaret T, Curtin WA. Scaling of dislocation strengthening by multiple obstacle types. Metall Mater Trans 2010;41:1954–60. https://doi.org/10.1007/s11661-010-0229-z.

[58] Bailey JE, Hirsch PB. The dislocation distribution, flow stress, and stored energy in cold-worked polycrystalline silver. Phil Mag 1960;5:485–97. https://doi.org/10.1080/14786436008238300.

[59] Feaugas X. On the origin of the tensile flow stress in the stainless steel AISI 316L at 300 K: back stress and effective stress. Acta Mater 1999;47:3617–32. https://doi.org/10.1016/S1359-6454(99)00222-0.

[60] Cottrell AH, Stokes RJ. Effects of temperature on the plastic properties of aluminium crystals. Proc R Soc Lond A Math Phys Sci 1955;233:17–34. https://doi.org/10.1098/rspa.1955.0243.

[61] Ogawa Y, Nishida H, Takakuwa O, Tsuzaki K. Hydrogen-enhanced deformation twinning in Fe-Cr-Ni-based austenitic steel characterized by in-situ EBSD observation. Mater Today Commun 2023;34:105433. https://doi.org/10.1016/j.mtcomm.2023.105433.

[62] San Marchi C, Somerday B, Robinson S. Permeability, solubility and diffusivity of hydrogen isotopes in stainless steels at high gas pressures. Int J Hydrogen Energy 2007;32:100–16. https://doi.org/10.1016/j.ijhydene.2006.05.008.

[63] Cottrell AH. Dislocations and plastic flow in crystals. New York: Oxford Univ. Press; 1953.

[64] Yoshinaga H, Morozumi S. The solute atmosphere round a moving dislocation and its dragging stress. Phil Mag: J Exp Theor Phys 1971;23:1367–85. https://doi.org/10.1080/14786437108217008.

[65] Epperly EN, Sills RB. Transient solute drag and strain aging of dislocations. Acta Mater 2020;193:182–90. https://doi.org/10.1016/j.actamat.2020.03.031.

[66] Alden TH. Theory of mobile dislocation density: application to the deformation of 304 stainless steel. Metall Trans A 1987;18:51–62. https://doi.org/10.1007/BF02646221.

[67] Estrin Y, Kubin LP. Local strain hardening and nonuniformity of plastic deformation. Acta Metall 1986;34:2455–64. https://doi.org/10.1016/0001-6160(86)90148-3.

[68] Ito T, Ogawa Y, Gong W, Mao W, Kawasaki T, Okada K, Shibata A, Harjo S. Role of solute hydrogen on mechanical property enhancement in Fe–24Cr–19Ni austenitic steel: in situ neutron diffraction study. 2024. in preparation.

[69] Anderson PM, Hirth JP, Lothe J. Theory of dislocations. third ed. Cambridge University Press; 2017.

[70] Basinski ZS, Foxall RA, Pascual R. Stress equivalence of solution hardening. Scripta Metall 1972;6:807–14. https://doi.org/10.1016/0036-9748(72)90052-X.

[71] Laplanche G, Bonneville J, Varvenne C, Curtin WA, George EP. Thermal activation parameters of plastic flow reveal deformation mechanisms in the CrMnFeCoNi high-entropy alloy. Acta Mater 2018;143:257–64. https://doi.org/10.1016/j.actamat.2017.10.014.

[72] Nabarro FRN. Stress equivalence in the theory of solution hardening. Proc Roy Soc Lond Math Phys Sci 1982;381:285–92. https://doi.org/10.1098/rspa.1982.0072.

[73] Kocks UF. Kinetics of solution hardening. Metall Trans A 1985;16:2109–29. https://doi.org/10.1007/BF02670415.

[74] Butt MZ, Feltham P. Solid-solution hardening. J Mater Sci 1993;28:2557–76. https://doi.org/10.1007/BF00356192.

[75] Nabarro FRN. Stress equivalence in the theory of solution hardening. Proc Roy Soc Lond Math Phys Sci 1982;381:285–92. https://doi.org/10.1098/rspa.1982.0072.

[76] Kirchheim R. Reducing grain boundary, dislocation line and vacancy formation energies by solute segregation. I. Theoretical background. Acta Mater 2007;55:5129–38. https://doi.org/10.1016/j.actamat.2007.05.047.

[77] Kirchheim R. Revisiting hydrogen embrittlement models and hydrogen-induced homogeneous nucleation of dislocations. Scripta Mater 2010;62:67–70. https://doi.org/10.1016/j.scriptamat.2009.09.037.

[78] Oriani RA. The diffusion and trapping of hydrogen in steel. Acta Metall 1970;18:147–57. https://doi.org/10.1016/0001-6160(70)90078-7.

[79] Atrens A, Fiore NF, Miura K. Dislocation damping and hydrogen pinning in austenitic stainless steels. J Appl Phys 1977;48:4247–51. https://doi.org/10.1063/1.323410.

[80] Yagodzinskyy Y, Ivanchenko M, Hänninen H. Hydrogen-dislocation interaction in austenitic stainless steel studied with mechanical loss spectroscopy. Solid State Phenom 2012;184:227–32. https://doi.org/10.4028/www.scientific.net/SSP.184.227.

[81] Zhou XW, Nowak C, Skelton RS, Foster ME, Ronevich JA, San Marchi C, Sills RB. An Fe–Ni–Cr–H interatomic potential and predictions of hydrogen-affected stacking fault energies in austenitic stainless steels. Int J Hydrogen Energy 2022;47:651–65. https://doi.org/10.1016/j.ijhydene.2021.09.261.

[82] Lothe J. The effect of temperature on dislocations with condensed impurity atmospheres. Theory of dislocation motion and dislocation break-away. Acta Metall 1962;10:663–70. https://doi.org/10.1016/0001-6160(62)90133-5.

[83] Girardin G, Delafosse D. Measurement of the saturated dislocation pinning force in hydrogenated nickel and nickel base alloys. Scripta Mater 2004;51:1177–81. https://doi.org/10.1016/j.scriptamat.2004.07.012.

[84] Friedel J. Dislocations. first ed. Pergamon Press; 1964.

[85] Moriyama J, Takakuwa O, Yamaguchi M, Ogawa Y, Tsuzaki K. The contribution of Cr and Ni to hydrogen absorption energy in Fe-Cr-Ni austenitic systems: a first-principles study. Comput Mater Sci 2024;232:112650. https://doi.org/10.1016/j.commatsci.2023.112650.

[86] Hirata K, Iikubo S, Ohtani H. First-principles calculations of the effects of Mn, Cr, and Ni on hydrogen diffusion in BCC, FCC, and HCP Fe. Tetsu-To-Hagane 2019;105:231–9. https://doi.org/10.2355/tetsutohagane.TETSU-2018-070.

[87] Ide N, Naito T, Asano S. Internal friction peak in FCC Fe-Cr-Ni alloys hydrogen-charged by gas-equilibration method. Jpn J Appl Phys, Part 1: J Appl Phys, Part 1 2005;44:8088–90. https://doi.org/10.1143/JJAP.44.8088.

[88] Perng T, Altstetter CJ. Effects of deformation on hydrogen permeation in austenitic stainless steels. Acta Metall 1986;34:1771–81. https://doi.org/10.1016/0001-6160(86)90123-9.

[89] Asano S, Shibata M, Tsunoda R. Internal friction due to hydrogen in austenitic stainless steels. Scripta Metall 1980;14:377–82. https://doi.org/10.1016/0036-9748(80)90330-0.

[90] Gavriljuk VG, Haänninen H, Smouk SYU, Tarasenko AV, Ullakko K. Internal friction in hydrogen-charged CrNi and CrNiMn austenitic stainless steels. Metall Mater Trans A Phys Metall Mater Sci 1996;27:1815–21. https://doi.org/10.1007/BF02651931.

[91] Whiteman MB, Troiano AR. The influence of hydrogen on the stacking fault energy of an austenitic stainless steel. Phys Status Solidi 1964;7:K109–10. https://doi.org/10.1002/pssb.19640070241.

[92] Rohatgi A, Vecchio KS, Gray GT. The influence of stacking fault energy on the mechanical behavior of Cu and Cu-Al alloys: deformation twinning, work hardening, and dynamic recovery. Metall Mater Trans 2001;32:135–45. https://doi.org/10.1007/s11661-001-0109-7.

[93] Kocks UF, Mecking H. Physics and phenomenology of strain hardening: the FCC case. Prog Mater Sci 2003;48:171–273. https://doi.org/10.1016/S0079-6425(02)00003-8.

[94] Astafurov SV, Maier GG, Melnikov EV, Moskvina VA, Panchenko MYu, Astafurova EG. The strain-rate dependence of the Hall-Petch effect in two austenitic stainless steels with different stacking fault energies. Mater Sci Eng 2019;756:365–72. https://doi.org/10.1016/j.msea.2019.04.076.

[95] Picu RC, Li R, Xu Z. Strain rate sensitivity of thermally activated dislocation motion across fields of obstacles of different kind. Mater Sci Eng 2009;502:164–71. https://doi.org/10.1016/j.msea.2008.10.046.

[96] Dong Y, Curtin WA. Thermally activated plastic flow in the presence of multiple obstacle types. Model Simulat Mater Sci Eng 2012;20:075006. https://doi.org/10.1088/0965-0393/20/7/075006.

[97] Van Den Beukel A. Theory of the effect of dynamic strain aging on mechanical properties. Phys Status Solidi 1975;30:197–206. https://doi.org/10.1002/pssa.2210300120.

[98] Yu H, Cocks ACF, Tarleton E. The influence of hydrogen on Lomer junctions. Scripta Mater 2019;166:173–7. https://doi.org/10.1016/j.scriptamat.2019.03.022.

[99] Aubert I, Delafosse D, Feaugas X, Aubert I, Saintier N, Olive JM. Hydrogen effects on the plasticity of FCC nickel and austenitic alloys. In: Proceedings of the 2008 international hydrogen conference. Materials Park, Ohio: ASM International; 2009. p. 78–87. https://www.researchgate.net/publication/256444957.

[100] Gilman JJ. Debris mechanism of strain-hardening. J Appl Phys 1962;33:2703–9. https://doi.org/10.1063/1.1702535.

[101] Zhou SJ, Preston DL, Louchet F. Investigation of vacancy formation by a jogged dissociated dislocation with large-scale molecular dynamics and dislocation energetics. Acta Mater 1999;47:2695–703. https://doi.org/10.1016/S1359-6454(99)00127-5.

[102] de Almeida LH, Le May I, Emygdio PRO. Mechanistic modeling of dynamic strain aging in austenitic stainless steels. Mater Char 1998;41:137–50. https://doi.org/10.1016/S1044-5803(98)00031-X.

[103] Fukai Y. Formation of superabundant vacancies in M–H alloys and some of its consequences: a review. J Alloys Compd 2003;356–357:263–9. https://doi.org/10.1016/S0925-8388(02)01269-0.

[104] Nagumo M, Takai K. The predominant role of strain-induced vacancies in hydrogen embrittlement of steels: overview. Acta Mater 2019;165:722–33. https://doi.org/10.1016/j.actamat.2018.12.013.

[105] Hatano M, Fujinami M, Arai K, Fujii H, Nagumo M. Hydrogen embrittlement of austenitic stainless steels revealed by deformation microstructures and strain-induced creation of vacancies. Acta Mater 2014;67:342–53. https://doi.org/10.1016/j.actamat.2013.12.039.

[106] Chiari L, Fujinami M. Recent studies of hydrogen-related defects in iron-based materials. ISIJ Int 2022;62. https://doi.org/10.2355/isijinternational.ISIJINT-2021-422. ISIJINT-2021-422.

[107] Komatsu A, Fujinami M, Hatano M, Matsumoto K, Sugeoi M, Chiari L. Straining-temperature dependence of vacancy behavior in hydrogen-charged austenitic stainless steel 316L. Int J Hydrogen Energy 2021;46:6960–9. https://doi.org/10.1016/j.ijhydene.2020.11.148.

[108] Xie D, Li S, Li M, Wang Z, Gumbsch P, Sun J, Ma E, Li J, Shan Z. Hydrogenated vacancies lock dislocations in aluminium. Nat Commun 2016;7:13341. https://doi.org/10.1038/ncomms13341.

[109] Zhu Y, Li Z, Huang M, Fan H. Study on interactions of an edge dislocation with vacancy-H complex by atomistic modelling. Int J Plast 2017;92:31–44. https://doi.org/10.1016/j.ijplas.2017.03.003.

[110] Zirkle T, Costello L, McDowell DL. Crystal plasticity modeling of hydrogen and hydrogen-related defects in initial yield and plastic flow of single-crystal stainless steel 316L. Metall Mater Trans 2021;52:3961–77. https://doi.org/10.1007/s11661-021-06357-8.

[111] Tateyama Y, Ohno T. Stability and clusterization of hydrogen-vacancy complexes in α−Fe : an ab initio study. Phys Rev B 2003;67:174105. https://doi.org/10.1103/PhysRevB.67.174105.

[112] Nazarov R, Hickel T, Neugebauer J. First-principles study of the thermodynamics of hydrogen-vacancy interaction in fcc iron. Phys Rev B 2010;82:224104. https://doi.org/10.1103/PhysRevB.82.224104.

[113] Nazarov R, Hickel T, Neugebauer J. Ab initio study of H-vacancy interactions in fcc metals: implications for the formation of superabundant vacancies. Phys Rev B 2014;89:144108. https://doi.org/10.1103/PhysRevB.89.144108.

[114] Ismer L, Park MS, Janotti A, Van de Walle CG. Interactions between hydrogen impurities and vacancies in Mg and Al: a comparative analysis based on density functional theory. Phys Rev B 2009;80:184110. https://doi.org/10.1103/PhysRevB.80.184110.

[115] Chiari L, Kojima K, Endo Y, Teshigahara H, Butterling M, Liedke MO, Hirschmann E, Attallah AG, Wagner A, Fujinami M. Formation and time dynamics of hydrogen-induced vacancies in nickel. Acta Mater 2021;219:117264. https://doi.org/10.1016/j.actamat.2021.117264.

[116] Echeverri Restrepo S, Lambert H, Paxton AT. Effect of hydrogen on vacancy diffusion. Phys Rev Mater 2020;4:113601. https://doi.org/10.1103/PhysRevMaterials.4.113601.

[117] Tanguy D, Wang Y, Connétable D. Stability of vacancy-hydrogen clusters in nickel from first-principles calculations. Acta Mater 2014;78:135–43. https://doi.org/10.1016/j.actamat.2014.06.021.